JACS
JOURNAL OF THE AMERICAN CHEMICAL SOCIETY

Article

pubs.acs.org/JACS

Massively Parallel and Highly Quantitative Single-Particle Analysis on Interactions between Nanoparticles on Supported Lipid Bilayer

Young Kwang Lee, Sungi Kim, Jeong-Wook Oh, and Jwa-Min Nam*

Department of Chemistry, Seoul National University, Seoul 151-747, South Korea

Supporting Information

ABSTRACT: Observation of individual single-nanoparticle reactions provides direct information and insight for many complex chemical, physical, and biological processes, but this is utterly challenging with conventional high-resolution imaging techniques on conventional platforms. Here, we developed a photostable plasmonic nanoparticle-modified supported lipid bilayer (PNP-SLB) platform that allows for massively parallel in situ analysis of the interactions between nanoparticles with single-particle resolution on a two-dimensional (2D) fluidic surface. Each particle-by-particle PNP clustering process was monitored in real time and quantified via analysis of individual particle diffusion trajectories and single-particle-level plasmonic coupling. Importantly, the PNP-SLB-based nanoparticle cluster growth kinetics result was fitted well. As an application example, we performed a DNA detection assay, and the result suggests that our approach has very promising sensitivity and dynamic range (high attomolar to high femtomolar) without optimization, as well as remarkable single-base mismatch discrimination capability. The method shown herein can be readily applied for many different types of intermolecular and interparticle interactions and provide convenient tools and new insights for studying dynamic interactions on a highly controllable and analytical platform.

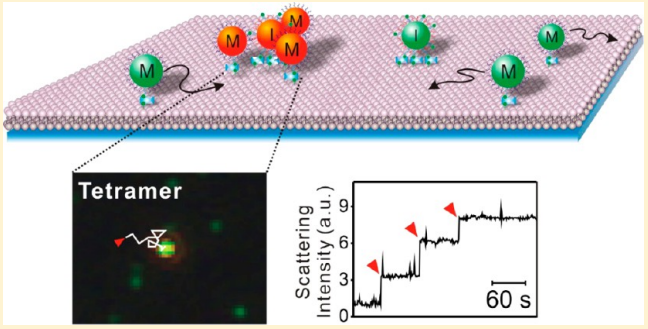

INTRODUCTION

Obtaining in situ information on dynamic interactions between nanoparticles or molecules with the highest possible resolution and accurate statistical data from individual particles over a large area is of paramount importance and is the fundamental basis for understanding and discovering scientific principles and their applications.[1−7] The single-nanoparticle-resolution in situ measurements provide time-dependent snapshots of the dynamic individual nanoparticles in action, and thus the heterogeneous interactions between nanoparticles can be elucidated and distinguished from the ensemble.[5,8] This can reveal direct and detailed information on colloidal nanocrystal growth and assembly mechanisms and molecular reaction kinetics.[8−11] However, conventional high-resolution imaging methods, including electron microscopy, typically provide static information on a limited number of structures without in situ data and require complicated setup and procedures under harsh conditions (e.g., vacuum).[12−14] Liquid transmission electron microscopy (TEM) techniques have been recently developed to observe interactions between individual nanoparticles in an aqueous environment in real time.[8,9] Nevertheless, the potential of the liquid TEM system for study of nanoparticle interactions is restricted to electron beam-triggered nanoparticle synthesis and assembly. The sealed liquid cell in a high vacuum condition does not permit changing reaction conditions, including buffer and introduction of chemical or biological molecules to trigger or manipulate nanoparticle reactions. Also, it is inevitable that particles and molecules are severely exposed to an electron flux, which affects the nanoparticle assembly kinetics and damages chemical and biomolecules in reactions. For these reasons, fluorophore-based single-molecule-level imaging and analysis methods have been heavily used in obtaining dynamic information on intermolecular interactions, but these methods suffer from the blinking and bleaching problems of fluorophores.[15] Further, discerning short-range molecular interactions of multiple components with fluorophore labels is highly challenging, and even with fluorescence resonance energy transfer, the measurable distance is limited to 10 nm and the interpretation becomes difficult for multicomponent systems.[15] Another important issue for reliable long-term single-nanoparticle analysis is that freely diffusing nanoparticles are repetitively focused in and out under optical microscopes because of their uncontrollable three-dimensional movements in solution, which makes it difficult to track the entire reaction trace for many particles (Figure 1a; Movie S1 in Supporting Information). Therefore, complex optical and mechanical systems are frequently required to reliably analyze dynamically moving nanoscale objects in solution state over a large focal depth for a long period of time, often with difficulties in simultaneously quantifying many objects in a reliable and reproducible fashion.[6,16,17] For all these reasons, it would be

Received: February 7, 2014
Published: February 12, 2014

dx.doi.org/10.1021/ja501225p | J. Am. Chem. Soc. 2014, 136, 4081−4088

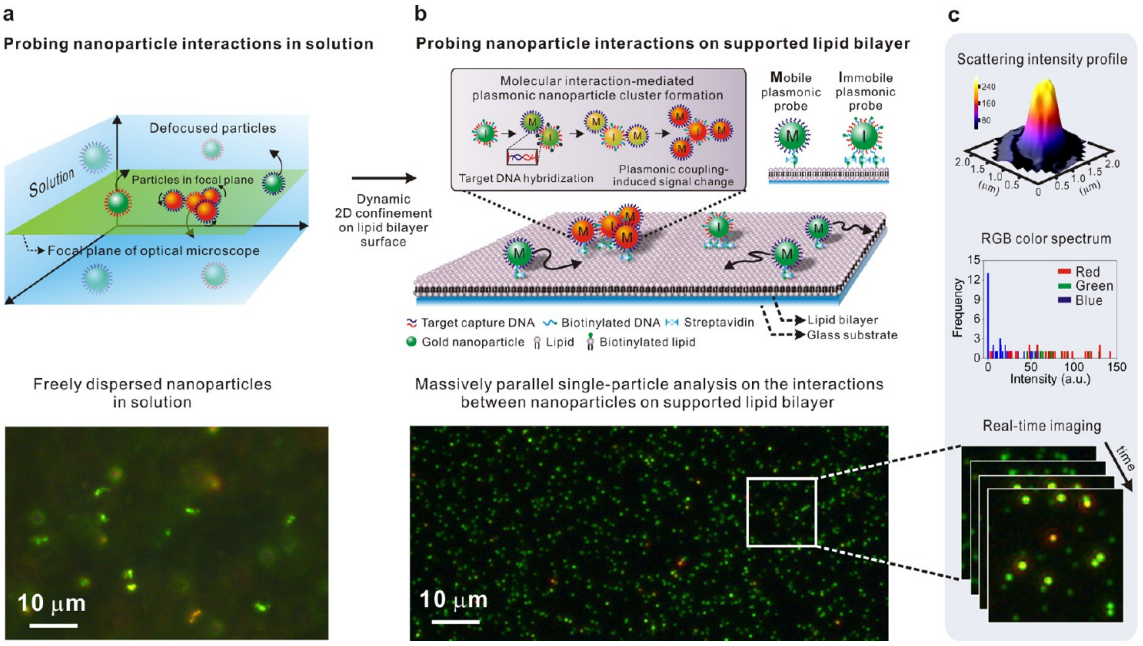

Figure 1. Single-nanoparticle-level in situ parallel imaging and analysis of dynamically tethered nanoparticles on a supported lipid bilayer. (a) (top) Schematic illustration of freely dispersed nanoparticles in uncontrolled three-dimensional motion. (bottom) Dark-field microscope image of 80 nm Au nanoparticles in solution (see Movie S1 in Supporting Information). Nanoparticles are repetitively focused in and out, which makes it difficult to reliably track individual nanoparticles for a long period of time. Freely diffusing 50-nm Au nanoparticles in solution are almost invisible because they generate scattering signals too weak to detect their fast free motions. (b) (top) Schematic illustration of dynamic two-dimensional confinement of plasmonic nanoparticles on lipid bilayer surface. Two different types of probes (mobile and immobile plasmonic probes) are tethered to a supported lipid bilayer. Target DNA hybridization induces two-dimensional cluster formation and plasmonic coupling. (bottom) Multiparallel in situ observation and analysis of supported lipid bilayer-tethered plasmonic nanoprobes via dark-field microscopy with single-nanoparticle resolution. A supported lipid bilayer modified with mobile and immobile probes is shown in Movie S3 in Supporting Information. (c) Quantitative analysis of single plasmonic nanoclusters based on dark-field microscope images. The scattering intensity and color spectrum, presented here, is obtained from the single plasmonic cluster marked with a white dashed line.

highly beneficial to develop a method that allows for in situ imaging and analysis of the interactions between freely moving nanoparticles with single-particle sensitivity. To obtain statistically meaningful information and derive new principles from studying interacting particles, one also needs to simultaneously track the interactions from multiple reaction sites with single-particle-level resolution.

In this work, to address the aforementioned challenges, we dynamically tethered plasmonic nanoparticles (PNPs) to a fluidic supported lipid bilayer (SLB) surface and controlled the mobility of PNPs by tuning the valency of particles. We then analyzed DNA hybridization-induced particle cluster growth dynamics with single-particle resolution and quantification on this platform, based on the detection of single-particle-level plasmonic coupling between interacting PNPs by dark-field microscopy (Figure 1b,c). The dynamic two-dimensional (2D) confinement of gold nanoparticles on a fluidic lipid bilayer surface allows for the effective imaging and tracking of all the nanoparticle movements and interactions for the entire reaction period, avoiding transient or permanent loss, which happens frequently in observation of freely diffusing nanoparticles in uncontrolled three-dimensional motion. Importantly, consecutive single-nanoparticle reactions resulted in quantified stepwise optical signal changes arising from plasmonic coupling. Interactions from multiple particle reaction sites were simultaneously monitored and analyzed; kinetic studies for the formation of dimeric, trimeric, and tetrameric nanoparticle clusters were performed; and a multiparallel dynamic single-particle analysis-based DNA detection assay was shown as an application of this method.

EXPERIMENTAL SECTION

Preparation of Small Unilamellar Vesicles. A supported lipid bilayer (SLB) was formed on a cover glass by the fusion of small unilamellar vesicles (SUVs) containing 97.4 mol % dioleoylphosphatidylcholine (DOPC), 0.1 mol % biotinylated dioleoylphosphatidylethanolamine (DOPE), and 2.5 mol % poly(ethylene glycol)−DOPE. The SUV solution was prepared by dissolving the appropriate amounts of lipids in chloroform. The lipid solution was evaporated in a 50 mL round-bottomed flask by use of a rotary evaporator. The lipid film was thoroughly dried under a stream of N_2. The dried mixture was resuspended in deionized (DI) water and subjected to three repetitive freeze−thaw cycles. The total lipid concentration was 2 mg·mL^{-1}. The solution was extruded more than 21 times through a polycarbonate (PC) membrane with a pore diameter of 100 nm at 25 °C. The resulting SUV solution was kept at 4 °C until use.

Functionalization of Au PNP Probes with DNA and Quantification of Biotin Valency. Thiolated oligonucleotides were reduced by incubation with 100 mM dithiothreitol (DTT) in 100 mM phosphate buffer (PB) solution (pH 8.0) for 2 h and separated on a NAP-5 column (GE Healthcare, Buckinghamshire, U.K.). For DNA functionalization, freshly reduced 4 μM oligonucleotides were mixed with 50 pM of 50-nm AuNPs and incubated at room temperature overnight. For immobile PNPs (I-PNPs), the molar ratio of SLB tethering sequence and target capture sequence was 200:600 (mole fraction of SLB tethering sequence was 0.25). For mobile PNPs (M-PNPs), the molar ratio was 1:799 (mole fraction of SLB tethering sequence was 0.00125). The solution was then adjusted to yield 10 mM phosphate buffer and 0.1% (w/v) sodium dodecyl sulfate (SDS). The adjusted solution was further incubated in an orbital shaker for 30

dx.doi.org/10.1021/ja501225p | J. Am. Chem. Soc. 2014, 136, 4081−4088

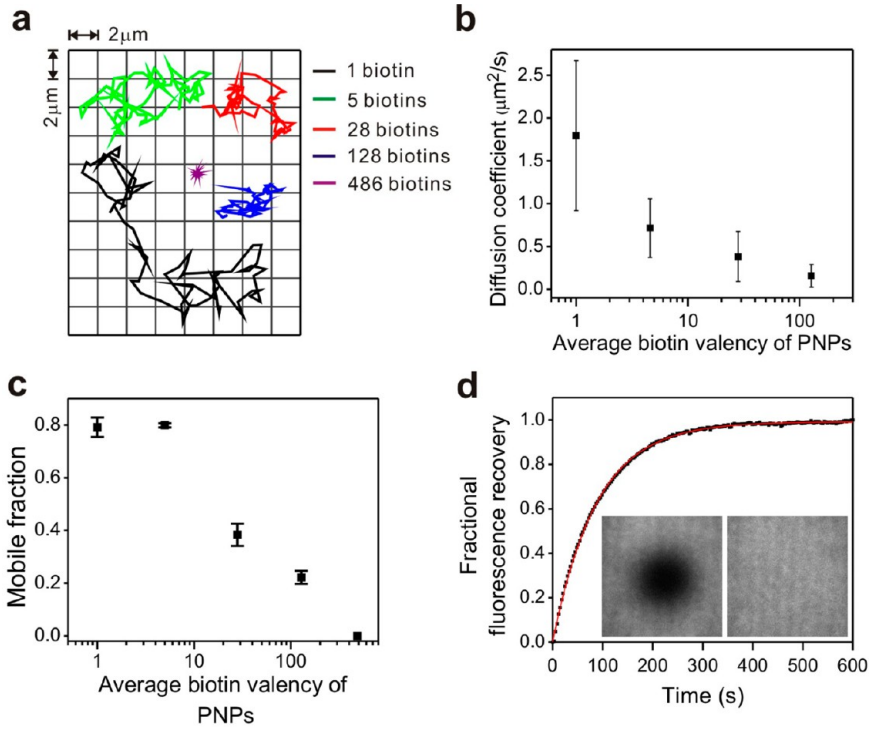

Figure 2. Biotin-valency-based control of nanoparticle mobility on a supported lipid bilayer. (a) Representative diffusion trajectories of nanoparticle probes with different biotin valencies. (b) Average diffusion coefficients of plasmonic probes on a supported lipid bilayer as a function of biotin valency (N = 100 particles). (c) Mobile fraction of lipid-tethered nanoparticle probes as a function of biotin valency. Each standard deviation was calculated from three independent measurements of 50 nanoparticles by the dark-field microscope. (d) Fluorescence recovery after photobleaching taken of a supported bilayer containing 1 mol % NBD-PC lipids. The plot is fitted to the equation $F(t) = A(1 - e^{-t\tau})$. The lateral diffusion coefficient is calculated as follows: $D = w^2\gamma_D/4t_{1/2}$, where w is the radius of the Gaussian bleaching light; γ_D is the correction factor, which depends on the bleach time and geometry of the bleaching light; and $t_{1/2}$ is the time of half-recovery. The values of w, γ_D, and $t_{1/2}$ used here were 18.3 μm, 1.12, and 61 s, respectively. (Insets) Bilayer after initial postphotobleaching and 6 min of recovery.

min, and six aliquots of 2 M NaCl were added to obtain a final NaCl concentration of 0.3 M with 0.05 M incremental steps. After each addition of 2 M NaCl, the solution was heated at 55 °C for 10 min and incubated for 30 min at room temperature. The DNA−AuNP mixture was allowed to stand overnight at room temperature and then the solution was centrifuged (4500 rpm, 10 min). The supernatant was eliminated and the precipitate was redispersed in DI water (this procedure was repeated three times). The DNA-functionalized AuNP solution was kept at 4 °C until use. For quantification of the number of SLB tethering sequences per AuNP, Cy3-labeled oligonucleotide-modified AuNPs were dissolved in 30 mM KCN solution. Measurement of fluorescence emission intensity of Cy3 was performed on an Acton spectrometer (Spectra Pro) with a Xe lamp (500 W) as an excitation source.

Preparation of Supported Lipid Bilayer and Modification of Au PNPs to SLB. The preparation of the SLB and tethering of Au PNPs to the SLB were done in a glass flow chamber. A flow chamber consists of the top and bottom glass substrates separated from each other by a 100-μm-thick thermoplastic spacer. Inlet and outlet holes were drilled on both ends of the top glass. The top slide glass was pretreated with 10 mg·mL^{-1} BSA in 0.15 M PBS for 1 h to make it inert to SLB deposition. The bottom cover glass was cleaned by sonicating for 10 min in chloroform, acetone, and ethanol. After sonication, the cover glass was washed with DI water and dried by a stream of N_2. Next, the bottom cover glass was pretreated with 1 M NaOH for 1 h and then thoroughly washed with DI water. The glass substrates were assembled with a sandwiched thermoplastic spacer by heating at 120 °C on a digital hot plate. The prepared SUV solution was mixed 1:1 (v/v) with 0.15 M PBS and introduced into the glass flow chamber through the inlet port. Approximately 70 μL of SUV solution was required to fill the flow channel. After 45 min of incubation at 25 °C, excess and unfused SUVs were washed out with 200 μL of DI water two times. Streptavidin (STV, 1 nM) in 0.15 M PBS solution was reacted with biotinylated SLB for 1 h after DI water in the flow channel was replaced with PBS. Unreacted STV was washed out with 0.15 M PBS, and then the flow channel was filled with 0.025 M PBS. Next, 2 pM I-PNP and 15 pM M-PNP probes were introduced and reacted for 10 min. Unbound PNPs were removed and unreacted STV binding sites were quenched by washing with 0.025 M PBS containing 1 μM free biotins. After 15 min, the buffer was exchanged to 0.15 M PBS. Typically, this procedure resulted in SLB-tethered I-PNP and M-PNP with the ratio 1:3.

Fabrication of Patterned SLB. For the DNA detection assays, a 120 × 120 μm^2 SLB was formed in a patterned gold film on a glass substrate. A gold pattern was fabricated by conventional photolithography and followed by lift-off process. Introduction of SUV solution yielded selective deposition of a SLB onto an exposed glass surface, because a gold surface is inert to SLB formation. After formation of SLB, gold surface was passivated with 2 mg·mL^{-1} bovine serum albumin and 10 mM carboxymethyl poly(ethylene glycol) dissolved in PBS to be resistant to nonspecific binding of PNPs and target DNA. Next, PNPs were tethered for use in DNA assay experiments.

Dark-Field Microscopy-Based in Situ Observation of PNP Probes and Optical Analysis. Movement and plasmonic coupling of SLB-tethered PNP probes were observed on a commercial dark-field microscope (Axiovert 200M, Carl Zeiss, Göttingen, Germany) with a 40× objective lens (NA 0.6) and AxiCam HRc color camera. All the image analysis procedures were conducted with ImageJ software (http://rsb.info.nih.gov/ij/). For tracking and trajectory analysis of individual SLB-tethered PNP probes, the MOSAIC plugin was used (http://www.mosaic.ethz.ch/Downloads/ParticleTracker).[18] The scattering intensity and RGB color spectra were analyzed by the basic intensity measurement and RGB color intensity splitting function of

dx.doi.org/10.1021/ja501225p | J. Am. Chem. Soc. 2014, 136, 4081−4088

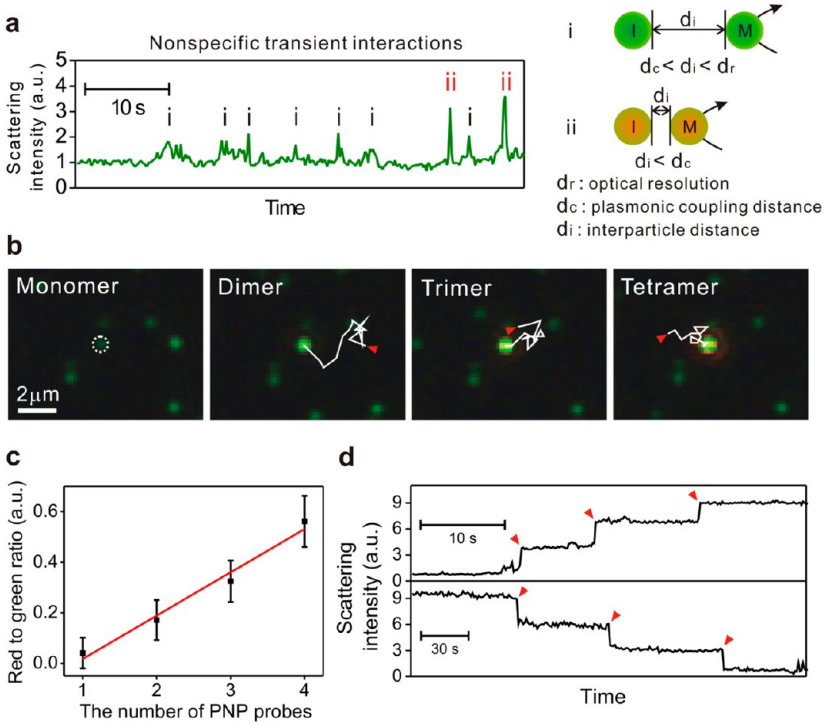

Figure 3. Optical analyses of interacting plasmonic nanoparticles on a supported lipid bilayer. (a) Time trace and schematic depiction of change in the scattering intensity for an immobile plasmonic probe site in the absence of target DNA sequence. (b) Dark-field microscopic images of target DNA hybridization-induced plasmonic nanoparticle clusters. The 15-step trajectories of mobile probes captured within an immobile probe site (white dashed circle) are highlighted with white solid lines, and red arrows indicate the starting positions of each trajectory. The time interval for each trajectory step is 0.188 s. The original movie is shown in Supporting Information (Movie S4). (c) Red-to-green ratio plot for the dark-field microscopic images of probe clusters as a function of the number of probes per cluster. (R^2 = 0.970, N = 30 clusters) (d) Representative time traces of the scattering intensity for (top) assembly and (bottom) disassembly processes of nanoparticle clusters.

ImageJ software, respectively. Cy3-modified STV and nitrobenzoxadiazolyl-labeled phosphatidylcholine (NBD-PC) lipid were observed by epifluorescence microscopy (TE-2000, Nikon, Tokyo, Japan) with 60× lens (NA 1.49) under 532 and 488 nm laser excitation, respectively. The brightness and contrast of microscope images are not adjusted unless it is mentioned in the figure caption.

RESULTS AND DISCUSSION

Dynamic Tethering of Plasmonic Nanoparticles on Lipid Bilayer Surface. Plasmonic nanoparticles were used in this approach because they efficiently scatter resonant light and are insusceptible to photobleaching and blinking.[19,20] Importantly, the plasmons of individual gold or silver nanoparticles (AuNPs or AgNPs) interact with each other in a distance-dependent manner,[21,22] and this forms a basic principle that underlies the measurements of molecular interactions on PNPs within several tens of nanometers by monitoring change in scattering intensity or spectral response without further labeling.[12,23−25] A supported lipid bilayer is a powerful and versatile platform, as it allows for synthesizing and controlling 2D fluidic surface on a solid substrate and incorporating a variety of species in a laterally mobile way.[26−34] By tethering nanoparticles to the SLB, we confined nanoparticles in the 2D focal plane of the optical microscope for efficient imaging and tracking of all the nanoparticles of interest while preserving the free motions of nanoparticles due to the fluidic nature of the SLB (Figure 1b). As tethered PNPs resonantly scatter the incident light and travel on the planar lipid bilayer surface, 2D diffusion trajectories and optical signals can be recorded in situ via the dark-field microscopy setup (Axiovert 200M, Carl Zeiss, Göttingen, Germany) with single-particle resolution (Figure 1b,c). The optical signal stability and spatial precision of our dark-field microscopy experiment are described in sections 2.1 and 2.2 in Supporting Information, respectively. The dark-field results proved that tethered PNPs were uniformly dispersed throughout the 2D membrane surface and showed excellent lateral mobility with free diffusion over the membrane surface (Movie S2, Supporting Information). This dynamic 2D confinement of particles and the use of PNP labels allow facilitation of efficient collisions between particles and in situ observation and analysis of nearly all the reactions between the molecules on nanoparticles.

Another important aspect of a high-resolution imaging method is the stable and reliable observation of interacting particles. To facilitate this, two types of DNA-modified plasmonic nanoparticle (DNA-PNP) probes with significant differences in lateral mobility were designed and tethered to the SLB surface: highly mobile (M-PNP) and nearly immobile (I-PNP) (Figure 1b). The scattering signal from a fixed I-PNP site can be stably monitored and analyzed, and M-PNPs diffuse into an I-PNP site to induce change in the plasmonic coupling-based light scattering signal. The mobility of PNP probes was controlled via the biotin valency of a probe by varying the mole fraction of SLB tethering sequence in the DNA modification procedure (see section 2.3 in Supporting Information). As PNPs become more multivalent, they travel shorter distance for a certain period of time (Figure 2a). Also, diffusion coefficients and mobile particle fraction get smaller, and all the particles were virtually immobile when the biotin valency reached 486 (Figure 2b,c; see section 2.4 in Supporting Information for the

dx.doi.org/10.1021/ja501225p | J. Am. Chem. Soc. 2014, 136, 4081−4088

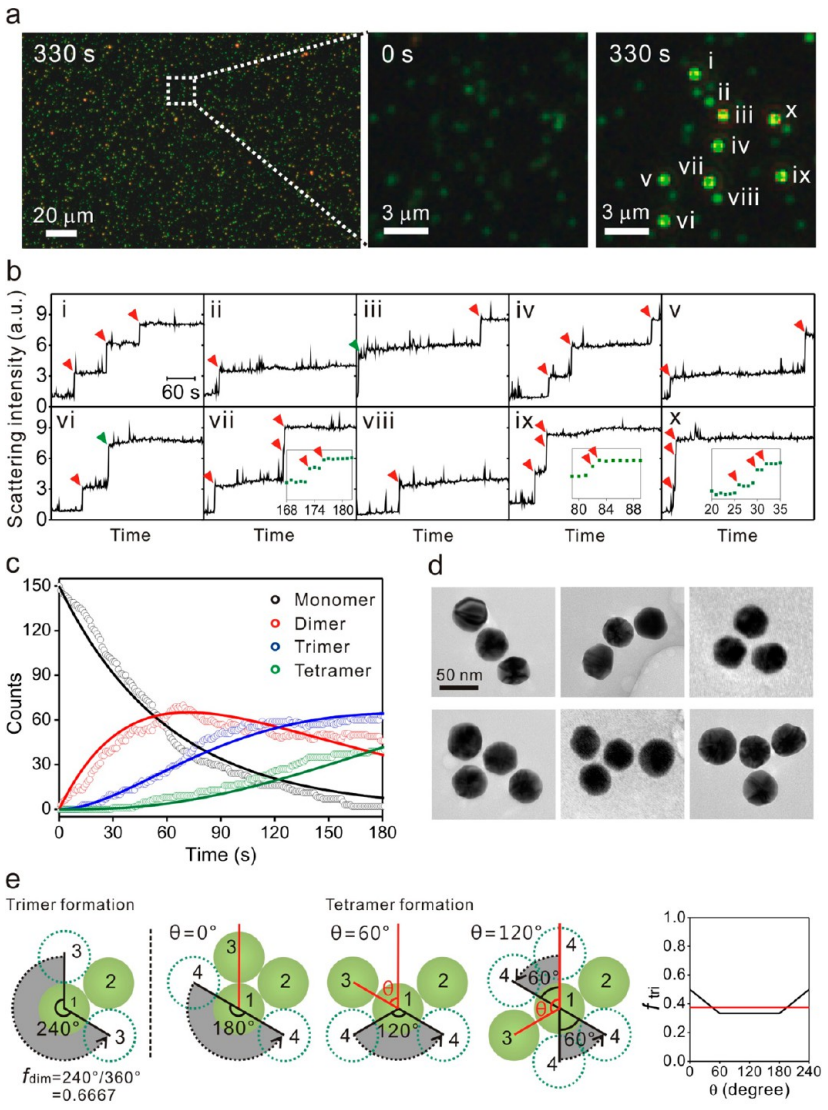

Figure 4. In situ multiparallel imaging and analysis of plasmonic nanoparticle clustering processes and the study on nanoparticle cluster growth kinetics. (a) Multiparallel in situ monitoring of DNA hybridization-induced plasmonic couplings of nanoparticle probes in a large SLB surface area. The left image was taken 330 s after the addition of 30 nM target DNA sequence. Magnified images of the white dashed area before (0 s) and after (330 s) the addition of target DNA sequence are shown. The original movie is shown in Supporting Information (Movie S6). (b) Time-dependent scattering intensity plots for 10 individual nanoparticle clustering reactions that are shown in the dark-field microscopic image in panel a. The scattering intensity was normalized to the average intensity of monomeric probes. The signal was recorded every 1 s for 330 s. Red arrows indicate monomer addition, and green arrows indicate simultaneous two-monomer addtion. (c) Reaction kinetics plot of plasmonic cluster growth with 30 nM target DNA (symbols). Each probe addition reaction was detected by monitoring the stepwide increase in scattering intesity of the growing clusters (N = 150 clusters). Cluster formation kinetics were fitted to a three-step consecutive reaction model (lines). (d) TEM images of clustered plasmonic nanoparticle probes assembled on the SLB. (e) Calculation of 2D steric hindrance factors for sequential addition of a plasmonic probe to a dimer to form a trimer, or to a trimer to form a tetramer. The gray regions represent the possible approach angle for the next particle addition. In tetramer formation, the steric hindrance factor is plotted as function of the accessible angle determined by relative position of the third particle (black solid line in the inset graph). The average f_{tri} is 0.375 (red dashed line).

detailed study). We observed and correlated a dark-field microscope image of multivalent PNPs and a fluorescence microscope image of Cy3-modified streptavidins (STVs) on the SLB to prove the position of PNPs matches with the position of locally concentrated STVs. The results show that two images are well matched to each other, suggesting that local accumulation of STVs under the multivalent PNP is responsible for the loss of particle mobility (Figure S4, Supporting Information). We also confirmed the complete lipid bilayer formation on a glass substrate by fluorescence recovery after photobleaching experiments (Figure 2d). The data fitting yielded a diffusion coefficient of 1.54×10^{-8} cm^2/s and 99% mobile fraction, demonstrating that the biotin-valency-based control of PNP mobility was conducted on the highly fluidic complete lipid bilayer. For M-PNP probes, 0.00125 mol fraction of the SLB tethering sequence was added to yield ~1 biotin valency. In the case of I-PNP probes, 0.25 mol fraction of the SLB tethering sequence was used.

Observation of Nanoparticle Interactions with Single-Nanoparticle Sensitivity. We differentiated short-range interactions below a few tens of nanometers on the basis of monitoring the scattering intensity changes originating from near-field plasmonic coupling between interacting nanoparticles by dark-field microscopy. The scattering intensity was analyzed

dx.doi.org/10.1021/ja501225p | J. Am. Chem. Soc. 2014, 136, 4081−4088

with ImageJ software by averaging an I-PNP site-centered circular area with a radius of 500 nm, which is similar to the optical resolution, d, of the microscopy setup ($d = \lambda/2\mathrm{NA}$; λ is the resonance wavelength of DNA-modified 50 nm AuNPs, 530 nm, and NA is the numerical aperture of the 40× objective lens, 0.6). In the absence of DNA-PNP-linking target DNA, M-PNP probes approached a fixed I-PNP site, but these PNPs were temporally overlapped because there is no specific interaction between DNA-PNPs in this case. Consequently, the scattering intensity of an I-PNP site was initially constant but fluctuated transiently as an M-PNP came within the optical diffraction limit (Figure 3a). Interestingly, two types of transient sharp rises in the signal were observed. In one case, which is more frequent, the scattering intensity was ∼2-fold higher than the initial value. This can be attributed to a distant optical overlapping, where two PNPs reside within the optical resolution but are not sufficiently close to each other to cause plasmonic coupling (Figure 3a-i). In the other case, ∼3.5-fold rise in the scattering intensity was observed, and the higher signal enhancement originated from the near-field interaction between two plasmonically coupled PNPs (Figure 3a-ii). It should be noted that most of these signal changes lasted for <0.5 s due to the absence of specific interactions between PNPs. In the next sets of experiments, we observed in situ DNA hybridization and dehybridization events that trigger the assembly and disassembly of DNA-PNP probes on the SLB and recorded the corresponding change in the scattering intensity at single-nanoparticle resolution in real time. In the presence of the target DNA sequence, paucivalent M-PNPs were captured by a multivalent I-PNP and formed a multiparticle cluster wherein an I-PNP was fixed and monitored as a tracking center. In the dark-field microscopic image, the assembly process was successfully resolved for observation of single-nanoparticle addition events. Particle-by-particle PNP cluster growth from monomer to tetramer was observed, and the trajectories of M-PNP probes that have been captured by an I-PNP probe are highlighted with white solid lines in Figure 3b. As the clusters evolved, we observed a stepwise change in both the scattering intensity and color in every M-PNP addition step to an I-PNP site (Movie S4, Supporting Information). Changes in the scattering efficiency and resonance wavelength arise from plasmonic coupling in the clustered AuNPs.[22,35,36] At 3 nM target DNA concentration, the reaction was finished in 15 min and many monomeric M-PNP probes were consumed to form the clusters. We found that nanoparticle interactions mediated by 2D diffusion on the lipid bilayer are much more efficient compared with interactions mediated by three-dimensional diffusion (see section 2.5 in Supporting Information). The cluster growth was usually restricted within a tetramer, and further growth beyond tetramer was hardly observed because there is a limited number of M-PNPs and also large steric hindrance between DNA strands on particles for the assembly of >4 particles in a single I-PNP site on the 2D surface (this will be discussed in detail later). Utilization of the fixed I-PNPs restricts the cluster growth pathway to particle-by-particle addition, by effectively eliminating the coalescence between particle clusters that produce unpredictable irregular 2D aggregates, and impairs the quantitative nature of this method (see section 2.6 and Movie S5 in Supporting Information for the coalescence process observed in M-PNP-modified SLB without I-PNPs). The plasmonic coupling between PNP probes caused a red shift in a resonance wavelength, and thus the plasmonically coupled green AuNPs turned into red in the dark-field microscopic image.[22,35,36] The plasmonic color change was analyzed by splitting and measuring RGB color intensity with ImageJ software (Figure 1c). As the cluster grew, green and red signals increased while blue signal remained constant. On the basis of these results, we plotted a red-to-green ratio graph, and a linear increase in the ratio was observed as the number of clustered particles increased (Figure 3c). The number of particles present in the clusters was defined by recording every monomeric particle attachment event. The color calibration standard is very useful to accurately and conveniently define and quantify the state of interparticle interactions and to differentiate the specific interaction-based plasmonic couplings from nonspecific optical overlaps.

Importantly, the particle-by-particle addition of M-PNP probes to an I-PNP site via target DNA recognition and hybridization was shown and quantified in the time trace of the scattering intensity (top graph in Figure 3d). The results show that the scattering signal intensity increased in a stepwise manner when each M-PNP was added to an I-PNP probe to sequentially form dimer, trimer, and tetramer. When high-salt PBS solution (167 mM Na^+) was replaced with low-salt PBS solution that contains much less salt (17 mM Na^+), M-PNPs were dehybridized and dissociated from I-PNP probes and freely diffused over the SLB surface again, which gave rise to a series of stepwise decreases in the scattering intensity (bottom graph in Figure 3d).

Massively Parallel Observation and Analysis of Cluster Formation Dynamics. Highly parallel in situ observations of multiple interactions were realized by the simultaneous analyses of individual plasmonic couplings of PNP probes over a large surface area (typically ∼30 000 μm^2; Figure 4a). The original movie of the zoomed-in image is shown in Supporting Information (Movie S6). Our in situ parallel particle cluster growth analysis results for 330-s observation (80-ms exposure time and 1-s time interval) show that, although a sequential particle-by-particle cluster growth was typically observed (Figure 4b-i, iv), many different clustering modes were observed with different clustering kinetics. Some probes formed dimers and did not grow further (Figure 4b-ii, viii). There is also a case where the probe cluster grew to form a trimer without growing further to form a tetramer (Figure 4b-v). Interestingly, the simultaneous addition of two probes to an I-PNP probe (Figure 4b-iii, vi) and back-to-back additions of two or three probes to an I-PNP probe within a very short time frame were also observed and resolved (Figure 4b-vii, ix, x; please see inset graphs for these cases). Importantly, with this in situ parallel single-particle resolution analysis capability, we studied DNA-hybridization-induced cluster-forming reaction kinetics. The scattering intensities of 150 individual I-PNP sites were simultaneously monitored for this purpose. The growth kinetics from monomer to tetramer

$$\text{monomer} \xrightarrow{k_1} \text{dimer} \xrightarrow{k_2} \text{trimer} \xrightarrow{k_3} \text{tetramer}$$

was fitted to a three-step consecutive reaction model by assuming that M-PNPs were present in excess compared to I-PNP monomers (Figure 4c; see section 2.8 in Supporting Information for details). The rate constants for dimer, trimer, and tetramer formation were estimated to be $k_1 = 0.0165$, $k_2 = 0.0116$, and $k_3 = 0.0061$ s^{-1}, respectively. This model explains the nanoparticle cluster growth kinetics within 180 s time. When the steric hindrance factor (f) is taken into account, the rate constants for trimer and tetramer formations can be expressed as $k_2 = f_{\mathrm{dim}}k_1$ and $k_3 = f_{\mathrm{tri}}k_1$, respectively. The steric

dx.doi.org/10.1021/ja501225p | J. Am. Chem. Soc. 2014, 136, 4081−4088

factors were calculated from the fitted rate constants (0.7030 for f_{dim} and 0.3697 for f_{tri}). We performed TEM measurement of PNP clusters assembled on the supported lipid bilayer (Figure 4d). The results show PNP clusters can be formed into different geometric configurations. On the basis of these observations, we geometrically calculated the steric factors for addition of the next PNP to a 2D dimer and a 2D trimer (geometrically calculated steric hindrance factors were f_{dim} = 0.6667 and f_{tri} = 0.3750; Figure 4e). These values are consistent with the steric factors obtained from the fitted rate constants, suggesting that the three-step consecutive reaction model successfully describes and explains the 2D cluster growth of DNA-modified PNP probes.

DNA Detection Assay and Single-Base Mismatch Discrimination. Finally, we drew the optical calibration standards for the number of reacted particles in the clusters, and on the basis of this standard curve, we performed a DNA detection assay with the PNP-tethered SLB platform. The calibration standard plots were obtained by analyzing 30 individual clusters simultaneously, and the number of particles in the cluster was confirmed by resolving and recording particle addition events. In order to avoid the simultaneous addition of multiple PNP probes within a single frame acquisition, the frame rate was elevated by 5.3 frames/s in this case. We plotted the averaged scattering intensities and found an excellent linear relationship with the number of clustered particles (R^2 value is 0.999, Figure 5a). Notably, the results exhibited narrow standard deviations, and we can clearly distinguish the clustered states. The corresponding distributions are shown in Figure S7 in Supporting Information. DNA detection was performed on 120 × 120 μm^2 SLB patterns embedded in a gold film (Figure 5b). PNP-modified SLBs were reacted for 4 h with different concentrations of target DNA ranging from 300 aM to 300 fM. All the samples, including the control sample, contained 300 fM noncomplementary DNA sequence to validate assay selectivity. We found that, at very low target DNA concentrations studied here, PNPs formed dimers only, without growing further to trimers and tetramers. I-PNP sites that showed the coupled dimer scattering intensity (>3.5-fold-enhancement; see Figure 5a) were counted as the detection signals (Figure 5b). The ΔPNP clusters were calculated by measuring the difference between the numbers of dimers before and after DNA hybridization reaction. The assay results shows there are target DNA concentration-dependent signal changes from 300 aM to 300 fM without optimization processes (Figure 5c). The dynamic range for DNA detection with our method is from 300 aM to 300 fM, but the clear detection limit in this case is 30 fM without optimization. Importantly, single-base-mismatched DNA sequence (solid red squares in Figure 5c) was clearly discriminated from target DNA sequence even at very low concentrations with our approach.

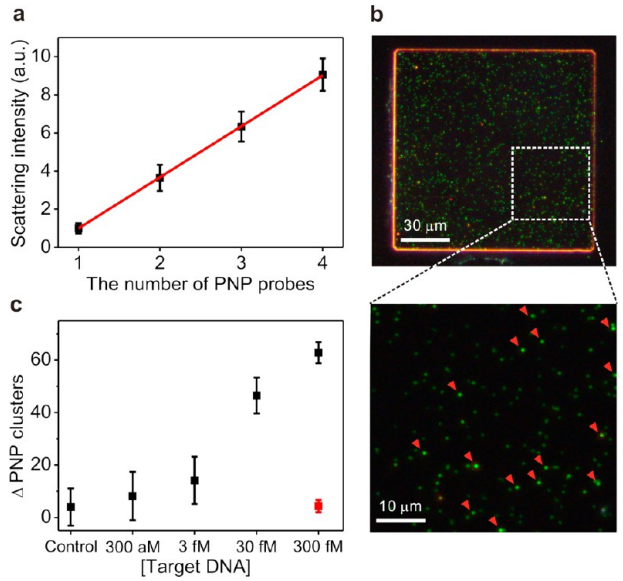

Figure 5. Dynamic plasmonic coupling-based DNA detection assay on the supported lipid bilayer. (a) Scattering intensity calibration standard as a function of the number of plasmonic probes in the cluster (R^2 = 0.999, N = 30 clusters). (b) PNP-modified patterned SLB with 300 fM target DNA (4 h incubation). Red arrowheads indicate PNP dimers. The brightness of the upper zoomed-out image was adjusted for clear visualization. (c) Plot of target DNA assay results as a function of target DNA concentration (black dots). The assay result for single-base-mismatched DNA sequence was plotted with a red dot. Each standard deviation was calculated from three independent samples.

CONCLUSIONS

The method reported herein should be applicable to any interaction pairs including DNA, RNA, proteins, and chemical ligands and in situ monitoring of heterogeneous membrane reactions and receptor clustering. Studying the interactions between molecules and particles is a key to understanding many scientific principles, and having methods for parallel in situ analysis of multiple dynamic interactions between nanoparticles with single-particle resolution will be highly beneficial and could lead to new information and insights for many complex interactions and reactions in physical and biological sciences.[37−42]

ASSOCIATED CONTENT

Supporting Information

Additional text and equations, seven figures, two tables, and six movies as described in the main text. This material is available free of charge via the Internet at http://pubs.acs.org.

AUTHOR INFORMATION

Corresponding Author

jmnam@snu.ac.kr

Notes

The authors declare no competing financial interest.

ACKNOWLEDGMENTS

J.-M.N. was supported by the National Research Foundation (NRF) of Korea (2011-0018198) and Center for BioNano Health-Guard funded by the Ministry of Science, ICT & Future Planning (MSIP) of Korea as Global Frontier Project (H-GUARD_2013M3A6B2078947). This work was also supported by the Pioneer Research Center Program (2012-0009586) through the NRF of Korea funded by the Ministry of Science, ICT, and Future Planning.

REFERENCES

(1) Kuzyk, A.; Schreiber, R.; Fan, Z.; Pardatscher, G.; Roller, E.; Högele, A.; Simmel, F. C.; Govorov, A. O.; Liedl, T. *Nature* **2012**, *483*, 311.

(2) Tan, S. J.; Campolongo, M. J.; Luo, D.; Cheng, W. *Nat. Nanotechnol.* **2011**, *6*, 268.

(3) Min, Y.; Akbulut, M.; Kristiansen, K.; Golan, Y.; Israelachvili, J. *Nat. Mater.* **2008**, *7*, 527.

(4) Li, D.; Nielsen, M. H.; Lee, J. R. I.; Frandsen, C.; Banfield, J. F.; Yoreo, J. J. D. *Science* **2012**, *336*, 1014.
(5) Zheng, H.; Smith, R. K.; Jun, Y.; Kisielowski, C.; Dahmen, U.; Alivisatos, A. P. *Science* **2009**, *324*, 1309.
(6) Cognet, L.; Tardin, C.; Boyer, D.; Choquet, D.; Tamarat, P.; Lounis, B. *Proc. Natl. Acad. Sci. U.S.A.* **2003**, *106*, 11350.
(7) Wang, Z.; Wang, F.; Peng, Y.; Zheng, Z.; Han, Y. *Science* **2012**, *338*, 87.
(8) Liu, Y.; Lin, X.-M.; Sun, Y.; Rajh, T. *J. Am. Chem. Soc.* **2013**, *135*, 3764.
(9) Liao, H.-G.; Cui, L.; Whitelam, S.; Zheng, H. *Science* **2012**, *336*, 1011.
(10) Reinhard, B. M.; Sheikholeslami, S.; Mastroianni, A.; Alivisatos, A.; Liphardt, J. *Proc. Natl. Acad. Sci. U.S.A.* **2007**, *104*, 2667.
(11) Christensen, S. M.; Bolinger, P.-Y.; Hatzakis, N. S.; Mortensen, M. W.; Stamou, D. *Nat. Nanotechnol.* **2012**, *7*, 51.
(12) Bigioni, T. P.; Lin, X.-M.; Nguyen, T. T.; Corwin, E. I.; Witten, T. A.; Jaeger, H. M. *Nat. Mater.* **2006**, *5*, 265.
(13) Tao, A.; Sinsermsuksakul, P.; Yang, P. *Nat. Nanotechnol.* **2007**, *2*, 435.
(14) Langille, M. R.; Zhang, J.; Personick, M. L.; Li, S.; Mirkin, C. A. *Science* **2012**, *337*, 954.
(15) Joo, C.; Balci, H.; Ishitsuka, Y.; Buranachai, C.; Ha, T. *Annu. Rev. Biochem.* **2008**, *77*, 51.
(16) Spille, J.-H.; Kaminski, T.; Königshoven, H.-P.; Kubitscheck, U. *Opt. Express* **2003**, *20*, 19697.
(17) Yu, J.; Wu, C.; Sahu, S. P.; Fernando, L. P.; Szymanski, C.; McNeill, J. *J. Am. Chem. Soc.* **2012**, *131*, 18410.
(18) Sbalzarini, I. F.; Koumoutsakos, P. *J. Struct. Biol.* **2005**, *151*, 182.
(19) Ueno, H.; Nishikawa, S.; Iino, R.; Tabata, K. V.; Sakakihara, S.; Yanagida, T.; Noji, H. *Biophys. J.* **2010**, *98*, 2014.
(20) Nan, X. L.; Sims, P. A.; Xie, X. S. *ChemPhysChem* **2008**, *9*, 707.
(21) Halas, N. J.; Lal, S.; Chang, W. S.; Link, S.; Nordlander, P. *Chem. Rev.* **2011**, *111*, 3913.
(22) Jain, P. K.; Huang, W. Y.; El-Sayed, M. A. *Nano Lett.* **2007**, *7*, 2080.
(23) Rong, G.; Wang, H.; Skewis, L. R.; Reinhard, B. M. *Nano Lett.* **2008**, *8*, 3386.
(24) Verdoold, R.; Gill, R.; Ungureanu, F.; Molenaar, R.; Kooyman, R. P. *Biosens. Bioelectron.* **2011**, *27*, 77.
(25) Monroe, M. R.; Daaboul, G. G.; Tuysuzoglu, A.; Lopez, C. A.; Little, F. F.; Unlü, M. S. *Anal. Chem.* **2013**, *85*, 3698.
(26) Mossman, K. D.; Campi, G.; Groves, J. T.; Dustin, M. L. *Science* **2005**, *310*, 1191.
(27) Tanaka, M.; Sackmann, E. *Nature* **2005**, *437*, 656.
(28) Chan, Y.-H. M.; Boxer, S. G. *Curr. Opin. Chem. Biol.* **2007**, *11*, 581.
(29) Tayebi, L.; Ma, Y.; Vashaee, D.; Chen, G.; Sinha, S. K.; Parikh, A. N. *Nat. Mater.* **2012**, *11*, 1074.
(30) Narui, Y.; Salaita, K. *Chem. Sci.* **2012**, *3*, 794.
(31) Sagle, L. B.; Ruvuna, L. K.; Bingham, J. M.; Liu, C.; Cremer, P. S.; Van Duyne, R. P. *J. Am. Chem. Soc.* **2012**, *134*, 15832.
(32) Yang, Y.-H.; Nam, J.-M. *Anal. Chem.* **2009**, *81*, 2564.
(33) Lee, Y. K.; Nam, J.-M. *Small* **2012**, *8*, 832.
(34) Lee, Y. K.; Lee, H.; Nam, J.-M. *NPG Asia Mater.* **2013**, *5*, e48.
(35) Wustholz, K. L.; Henry, A. I.; McMahon, J. M.; Freeman, R. G.; Valley, N.; Piotti, M. E.; Natan, M. J.; Schatz, G. C.; Van Duyne, R. P. *J. Am. Chem. Soc.* **2010**, *132*, 10903.
(36) Yan, B.; Boriskina, S. V.; Reinhard, B. M. *J. Phys. Chem. C* **2011**, *115*, 10903.
(37) Cho, E. C.; Zhang, Y.; Cai, X.; Moran, C. M.; Wang, L. V.; Xia, Y. *Angew. Chem., Int. Ed.* **2013**, *52*, 1152.
(38) Joh, D. Y.; Kinder, J.; Herman, L. H.; Ju, S. Y.; Segal, M. A.; Johnson, J. N.; Chan, G. K.; Park, J. *Nat. Nanotechnol.* **2011**, *6*, 51.
(39) Wang, F.; Han, Y.; Lim, C. S.; Lu, Y.; Wang, J.; Xu, J.; Chen, H.; Zhang, C.; Hong, M.; Liu, X. *Nature* **2010**, *463*, 1061.
(40) Das, A.; Li, T.; Nobusada, K.; Zeng, Q.; Rosi, N. L.; Jin, R. *J. Am. Chem. Soc.* **2012**, *134*, 20286.
(41) Bamrungsap, S.; Chen, T.; Shukoor, M. I.; Chen, Z.; Sefah, K.; Chen, Y.; Tan, W. *ACS Nano* **2012**, *6*, 3974.
(42) Qian, X.; Peng, X. H.; Ansari, D. O.; Yin-Goen, Q.; Chen, G. Z.; Shin, D. M.; Yang, L.; Young, A. N.; Wang, M. D.; Nie, S. *Nat. Biotechnol.* **2008**, *26*, 83.